# Recovery of lanthanum cations by functionalized magnetic multi-walled carbon nanotube bundles†

Lijinhong Huang,[ab] Lihong Liu, [ID] *[b] Wanfu Huang,*[c] Bingxin Zhao,[c] Zhangfeng Shen,[d] Yaqing Bao[c] and Hussein Znad[b]

Rare-earth elements (REE), including La, are critical raw materials in many technological advancements. Collection of physically adsorbed REEs on clay minerals can be realized first by ion-exchange leaching, followed by adsorption enrichment. Ever increasing demand and limited resources of REEs have fueled the development of nanostructured adsorbents. In this paper, multi-walled carbon nanotubes (MWCNTs) were purified using concentrated $H_2SO_4$ and $HNO_3$, then coupled with magnetic $Fe_3O_4$ nanoparticles to make low concentration La ion extraction from water possible. The $MWCNT@Fe_3O_4$ composites were further crosslinked with 0.1 wt% epichlorohydrin and functionalized with 0.5 wt% carbon disulfide to achieve a $La^{3+}$ adsorption capacity of 23.23 mg $g^{-1}$. We fully probed the morphology, crystallinity, chemical composition, and magnetic properties of the as-prepared adsorbent by scanning/transmission electron microscopy, X-ray diffractometry, X-ray photoelectron spectroscopy, vibrating-sample magnetometry, and thermal gravimetry. These results indicated that the $MWCNT@Fe_3O_4$ nanohybrid may be a promising candidate for recovering La ions from aqueous solutions.

## Introduction

The rare earth elements (REE) comprise a group of fifteen lanthanides of the periodic table (IIIB metals) plus scandium and yttrium. The unique chemical, electrical, magnetic, optical, and luminescent properties of REE render them essential components to high-tech and green-energy products, such as nuclear medicines, lasers, electronic displays, high strength alloys, radar, and vehicle catalytic converters.[1] The extraction of REE from commercially significant bastnäsite ores involves large up-front capital investments, high energy costs and environmental risks.[2] An alternative source to obtain REE is from weathered crust elution-deposited rare earth ores, also known as ion-adsorption clays.[3] The clay deposits contain 0.05 to 0.2 wt% rare earths, out of which 60–90% occur as physically adsorbed species recoverable by simple ion-exchange leaching with concentrated monovalent cations.[4] The free rare earth ions ($RE^{3+}$) are then precipitated with oxalic acid and converted to RE oxides *via* 900 °C calcination. However, when $RE^{3+}$

concentrations are low, the use of adsorbents for ion pre-concentrating is necessary.[5] Indeed, adsorption is the most explored method due to its simplicity and wide-ranging availability for low concentration REE recovery from electronics waste, brines, and various industrial wastes.

Biosorption based on a variety of biomaterials such as algae, fungi, bacteria, *etc.*, have been proposed for the recovery of $RE^{3+}$, but more efforts are needed to solve the problematic nature of biomass regeneration. Recently, bulky zeolite, clay, active carbon, and nanomaterials (NMs) have received increasing attention. Numerous non-magnetic $SiO_2$, $TiO_2$ and carbon based NMs have been reported for this type of application.[6] In particular, the large surface areas, high porosity, hollow and layered structures have made multi-walled carbon nanotubes (MWCNTs) an ideal adsorption material. On the one hand, the high adsorption capacity of MWCNTs stems from the large specific surface area, hence having more active or binding sites. On the other hand, the sorption of $RE^{3+}$ is primarily controlled by electrostatic forces, which are associated with negatively charged surface function groups.[7] Oxidized MWCNTs and graphene oxides have emerged as excellent metal ion adsorbents due to possessing many oxygen donor groups (*e.g.* hydroxyl, carbonyl and carboxyl) on their surfaces.[8,9]

The sorption performance of MWCNTs relies on their homogeneous dispersion. It is a challenge to remove the suspended MWCNTs from the aquatic phase. Experiments have been conducted to explore the use of magnetism as an effective means of separating the spent adsorbents. Magnetite ($Fe_3O_4$) and maghemite ($\gamma$-$Fe_2O_3$) are commonly incorporated with

*[a]School of Architecture and Design, Jiangxi University of Science and Technology, Ganzhou, China*

*[b]Faculty of Science and Engineering, WA School of Mines: Minerals, Energy and Chemical Engineering, Curtin University, WA, Australian. E-mail: lihong.liu@curtin.edu.au*

*[c]School of Resource and Environmental Engineering, Jiangxi University of Science and Technology, Ganzhou, China. E-mail: sim2008@sina.com*

*[d]College of Biological, Chemical Science and Engineering, Jiaxing University, China*

† Electronic supplementary information (ESI) available. See DOI: 10.1039/d0ra09902c

MWCNTs for adsorption removal of $Cr^{6+}$, $Pb^{2+}$, $Mn^{2+}$, $Cu^{2+}$ and organic cationic dyes.[10–13] However, few studies on the interaction between $RE^{3+}$ and magnetic MWCNTs has been reported which serves as the primary motivation of this work.

The overall objective of this research is to modify MWCNT to become a magnetically retrievable adsorbent that can efficiently recover REEs. Firstly, an attempt has been made to purify and oxidize MWCNT to overcome the hydrophobicity issue by the introduction of hydroxyl and carboxyl groups. Polyvinyl alcohol was employed to assemble MWCNT@$Fe_3O_4$. Upon the surface treatment, epichlorohydrin (ECH) was used to cross-link the CNTs through reaction with –OH. There are sparse studies regarding the use of magnetic MWCNTs–ECH hybrids for the removal of $La^{3+}$. It was expected that the 3D structure formation can enhance the mechanical strength of the adsorbent in harsh acid solution. Functionalized CNTs-based nanomaterials have exhibited an enhanced performance for energy-related oxygen evolution reaction and water oxidation.[14–16] In this study, MWCNT@$Fe_3O_4$ with $CS_2$ was constructed based on the innate affinity of $S^{2-}$ for metal ions.[17] The ability of the as-prepared adsorbent to recover $La^{3+}$ was evaluated under a range of ECH and $CS_2$ weight ratios. Effective $La^{3+}$ sorption was accomplished with 0.1 wt% ECH and 0.5 wt% carbon disulfide.

# Experimental section

## Materials and chemicals

Pristine multi-walled carbon nanotubes (MWCNTs) and $Fe_3O_4$ nanoparticles were purchased from Shenzhen Nanoport Co., Ltd. and Aladdin, respectively. Concentrated sulfuric acid/nitric acid and absolute ethyl alcohol were purchased from Xilong Science Co., Ltd. Polyvinyl alcohol (PVA-1788) and epichlorohydrin (ECH) were obtained from Shanghai McLean Biochemical Co. Ltd. Analytical grade sodium hydroxide and carbon disulfide were procured from Sinopharm Chemical Reagent Co., Ltd. All the products were used as received.

## Modification and functionalization of multi-walled carbon nanotubes

To remove carbonaceous and metallic impurities, at room temperature, 6 g of MWCNTs were ultrasonically treated in a mixture of 180 mL concentrated sulphuric acid (98%) and 60 mL concentrated nitric acid (70%) for 35 min followed by refluxing under 500 rpm magnetic stirring at 80 °C for 3 h. The suspension was settled for 12 h then diluted with 1.92 L DI water. After 10 h settlement, the supernatant fluid was decanted off and the precipitate was washed with DI water for several times to reach neutral pH. After ethanol washing 4 more times, the product was vacuum dried at 80 °C for 12 h.

The magnetic $Fe_3O_4$ NPs were embedded within MWCNT bundles that were crosslinked by ECH. Briefly, 1 g of purified MWCNT in 30 mL absolute ethanol was ultrasonically treated for 1 h. At the same time, 1 g of PVA in 30 mL ultrapure water was magnetically stirred at 500 rpm for 1 h at room temperature then mixed with the MWCNT suspension slowly. After that, 1 g of $Fe_3O_4$ powder was added and the mixture was magnetically

stirred for 3 h to obtain a homogenous suspension. 0.1 M NaOH (6 mL) was slowly injected into the mixture to ionize the MWCNT hydroxyl groups. After 12 h settlement, the precipitate was washed with ultrapure water till reaching neutral pH. To crosslink the MWCNT thus embedding $Fe_3O_4$ NPs within the MWCNT matrix, 100 mL ECH with various concentrations were mixed with the assembled MWCNT@$Fe_3O_4$ composites and then stirred for 4 h at room temperature. After decantation, the precipitate was washed with ultrapure water then dried in −0.1 MPa at 70 °C for 12 h.

To functionalize MWCNT@$Fe_3O_4$ with S motif, 100 mL $CS_2$ with different concentrations were mixed with 1 g MWCNT@$Fe_3O_4$ in water. After 12 h stirring at 400 rpm, the precipitate was collected by decantation and washed with ultrapure water several times then dried in −0.1 MPa at 70 °C for 12 h.

## Orthogonal array (OA) design for optimizing concentrations of ECH and $CS_2$

In this study, ECH and $CS_2$ concentrations were two identified factors to have large effects on the adsorption capacity of MWCNT@$Fe_3O_4$. We first determined ECH concentration (factor $A$, from 0.05 to 10%) influence by fixing $CS_2$ concentration at 0.5%. Secondly, we evaluated $CS_2$ concentration (factor $B$, from 0.1 to 2%) influence by fixing ECH concentration at 0.1%. Based on these preliminary results, in order to realize prompt evaluation of optimal concentrations of ECH and $CS_2$ for the maximum $La^{3+}$ adsorption, a Taguchi $OA_9$ ($3^2$) matrix, which is an orthogonal array of two factors and 3 levels, was then employed to design experimental conditions as shown in Table 1.

Nine trials were conducted as per the level combinations. Optimal conditions were obtained after the experiments and data analysis, including range analysis and analysis of variance.

## Materials characterizations

The morphology of the prepared samples was observed by scanning electron microscopy (SEM, Quanta FEG 250). The crystal structure of the composites was characterized by powder X-ray diffraction (XRD, X'Pert Pro MPD) using Cu-K$\alpha$ radiation ($\lambda = 0.15404$ nm). The data was collected under a continuous scan mode between 10 and 90° with a step size of 0.02° and a scan rate of 2° min$^{-1}$. The current and voltage were set at 30 mA and 40 kV, respectively. The Brunauer–Emmett–Teller (BET) specific surface areas of as-prepared samples were measured by $N_2$ adsorption–desorption isotherm with a Quantachrome NOVA touch LX4 apparatus (Quantachrome Autosorb-IQ, USA).

Table 1 Levels and factors affecting the $La^{3+}$ adsorption

| | ECH concentration ($A$, wt%) | $CS_2$ concentration ($B$, wt%) |
|---|---|---|
| Level 1 | 0.1 | 0.1 |
| Level 2 | 1.0 | 0.5 |
| Level 3 | 5.0 | 1.0 |
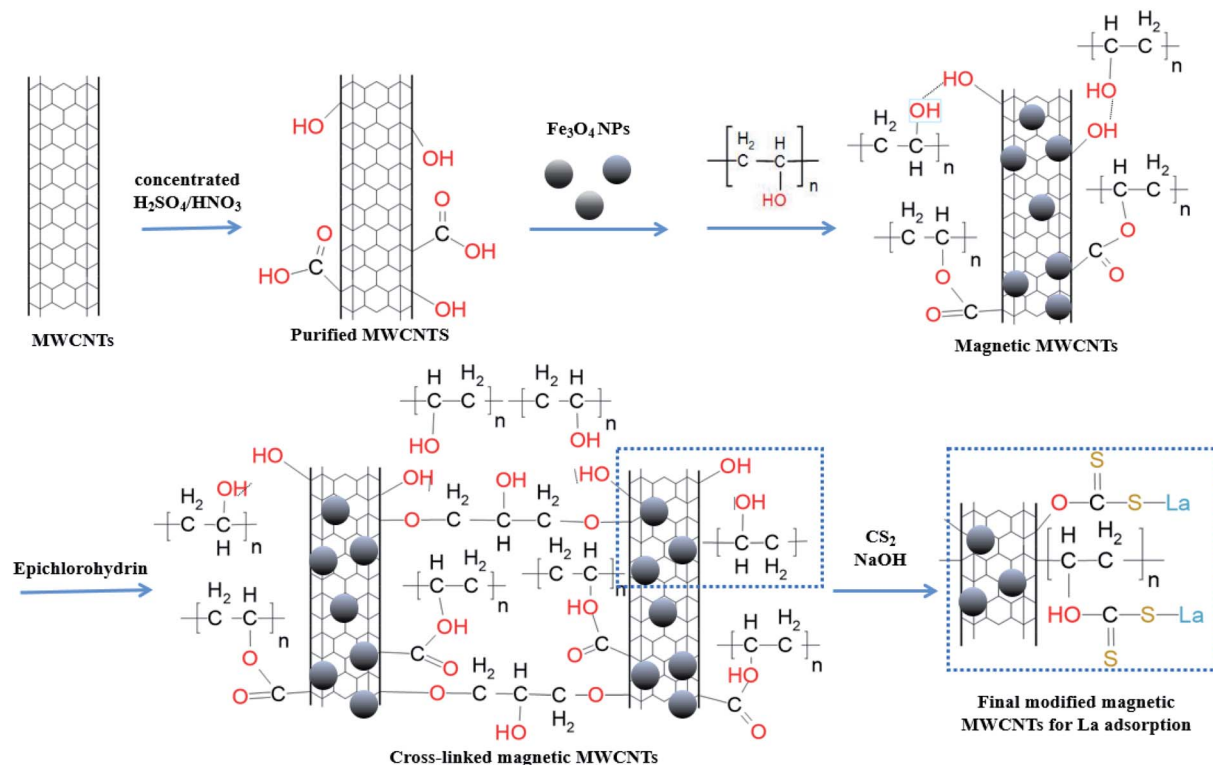
**Scheme 1** Synthesis of sulfur functionalized magnetic multi-walled carbon nanotubes.

The chemical compositions and bonds were studied by X-ray photoelectron spectroscopy (XPS, ESCALAB 250Xi K-alpha, Thermo Fisher Scientific) with Al Kα X-ray at 15 kV and 150 W. Fourier transform infrared (FTIR) spectra were measured by using a VERTEX70 spectrometer. Thermogravimetric analysis (TGA; Mettler-Toledo) was performed using a simultaneous differential thermal analysis (DTA). A heating rate of 5 °C min$^{-1}$ was used from room temperature to 900 °C under atmospheric air. Vibrating sample magnetometer (VSM) (Model: Lake shore 7400, United States) was employed to study the hysteresis loops and the magnetic properties of the magnetite nanocomposites.

### La$^{3+}$ adsorption and reusability tests

The batch adsorption of La$^{3+}$ was evaluated by continuously stirring the samples (200 mg modified MWCNT@Fe$_3$O$_4$ with 50 mL of 100 mg L$^{-1}$ La(NO$_3$)$_3$ solution) at 150 rpm in a thermostatic shaker, at 25 ± 2 °C for 12 h. The initial pH was 5. After the completion of adsorption, the solutions were centrifuged, and the residual concentration of La$^{3+}$ in the supernatant was detected on a Perkin Optima 8300 inductively coupled plasma-optical emission spectrometry (ICP-OES).

To investigate the reusability, sequential adsorption–desorption experiments in batch mode were carried out for three cycles. The adsorbents loaded with La$^{3+}$ were placed in 2 mol L$^{-1}$ H$_2$SO$_4$ and vibrated for 60 min. The La$^{3+}$ concentration in the aqueous phase and stripping acid were determined using ICP-OES.

## Results and discussion

As depicted in Scheme 1, firstly, MWCNTs were purified by concentrated HNO$_3$/H$_2$SO$_4$. MWCNT@Fe$_3$O$_4$ composites were then prepared *via* surface deposition and epichlorohydrin (ECH) cross-linking process. Finally, CS$_2$ molecules were introduced to add S motif for enhanced metal ion adsorption. We systemically investigated the influence of ECH and CS$_2$ concentrations in the following sections.

### Effect of epichlorohydrin (ECH) concentration on La$^{3+}$ sorption

Epichlorohydrin (ECH) reacts with –OH groups on the surface of carbon nanotubes to form a three-dimensional network through ether bonds.[18] It is well documented such chemical crosslink can enhance the mechanical strength and maintain the adsorption performance in harsh acidic solution. Fig. 1 shows the effect of ECH concentration on the extent of sorption of La$^{3+}$. An increase in the cross-linker concentration from 0.05 to 1% led to an improved La$^{3+}$ uptake, which may be correlated to the extra pores formed among MWCNT bundles. However, the uptake of La$^{3+}$ declined when ECH concentration increased from 5 to 8%, implying that steric effects likely play a role due to excessive cross-linking. When 10% ECH was used, La$^{3+}$ adsorption increased a bit but still lower than the 1% ECH cross-linked MWCNT@Fe$_3$O$_4$. This may occur due to self-crosslinking of the hydroxyl group of ECH at the C2 position and/or hydrolysis of ECH under alkaline condition.[19]
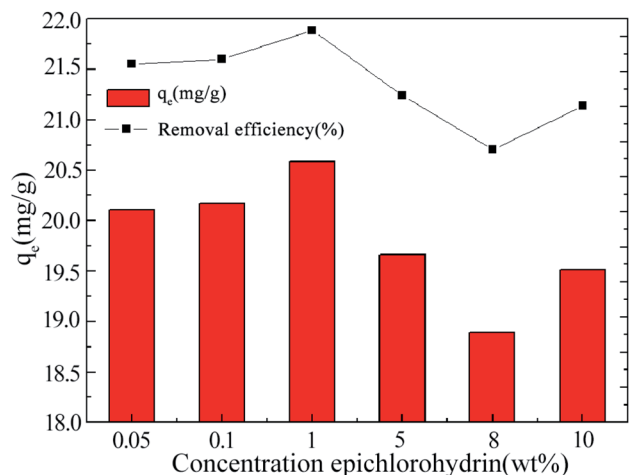
Fig. 1 La(ɪɪɪ) adsorbed by functionalized MWCNT@Fe$_3$O$_4$ with variable epichlorohydrin (ECH) concentrations, [CS$_2$] = 0.5 wt%.

## Effect of CS$_2$ concentration on La$^{3+}$ sorption

Sulfur-doped carbon materials have been extensively explored in metal adsorption due to the soft acid–soft base interactions between metal ions and sulfur functionalities. For example, Saha has investigated aqueous phase adsorption of Hg, Pb, Cd, and Ni ions by sulfur-functionalized ordered mesoporous carbons.[20] Besides physisorption in the pores of the parent carbon, sulfur is hypothesized to increase surface polarity and enhance negative charge on the sorbent materials to attract the metal cations.

Effect of CS$_2$ concentration on La$^{3+}$ adsorption by modified MWCNTs was investigated at fixed ECH concentration of 0.1 wt% (Fig. 2). Sorption of La$^{3+}$ increased with increase in CS$_2$ concentration from 0.1 wt% to 0.5 wt%, as more thiol groups for S–La$^{3+}$ complex were formed on carbon surface after reaction with OH groups (Scheme 1). When the concentration of CS$_2$ reached to 1.0 wt%, OH groups were already consumed and most of CS$_2$ molecules were physically tangled with MWCNTs,
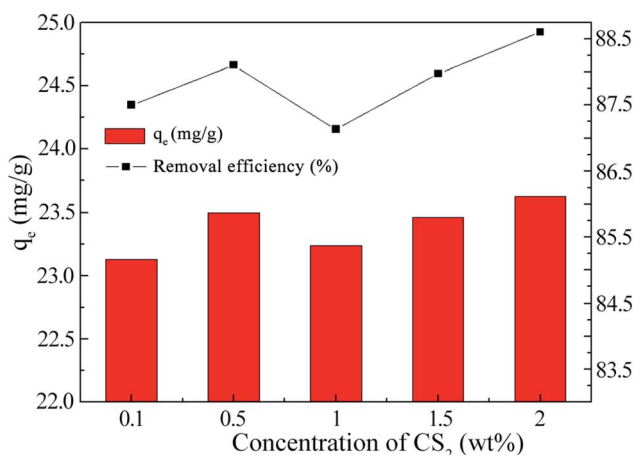


Fig. 2 La(ɪɪɪ) adsorbed by functionalized MWCNT@Fe$_3$O$_4$ with variable CS$_2$ concentrations, [ECH] = 0.1 wt%.

**Table 2** Orthogonal test results and range analysis of data

| Serial number | ECH, wt% A factor | CS$_2$, wt% B factor | Removal rate% | Adsorption capacity (mg g$^{-1}$) |
|---|---|---|---|---|
| 1 | 0.10% | 0.10% | 56.82 | 11.36 |
| 2 | 0.10% | 0.50% | 65.98 | 13.20 |
| 3 | 0.10% | 1.00% | 63.79 | 12.76 |
| 4 | 1.00% | 0.10% | 58.43 | 11.686 |
| 5 | 1.00% | 0.50% | 62.265 | 12.453 |
| 6 | 1.00% | 1.00% | 57.91 | 11.58 |
| 7 | 5.00% | 0.10% | 62.14 | 12.43 |
| 8 | 5.00% | 0.50% | 60.27 | 12.06 |
| 9 | 5.00% | 1.00% | 66.13 | 13.225 |
| $K_1$ | 186.59 | 177.39 | | |
| $K_2$ | 178.605 | 188.515 | | |
| $K_3$ | 188.54 | 187.83 | | |
| $\overline{K_1}$ | 62.20 | 59.13 | | |
| $\overline{K_2}$ | 59.54 | 62.84 | | |
| $\overline{K_3}$ | 62.85 | 62.61 | | |
| $R$ | 3.31 | 3.71 | | |

therefore reducing the adsorption effect. The final composite functionalized with 0.5 wt% CS$_2$ exhibited ideal La$^{3+}$ adsorption at 23.23 mg g$^{-1}$.

## Optimization of ECH and CS$_2$ concentrations by Taguchi approach

According to the OA$_9$ matrix, nine experiments were performed, and their adsorption results were shown in Table 2.

For range analysis, we first calculated $K_{ji}$ and $\overline{K_{ji}}$. $K_{ji}$ is the sum of the evaluation indexes of all levels ($i$, $i$ = 1, 2, 3) in each factor ($j$, $j$ = A, B). $\overline{K_{ji}}$ is the mean value of $K_{ji}$. For example, $K_{1A}$ = 56.82 + 65.98 + 63.79 = 186.59. $\overline{K_{1A}} = \dfrac{K_{1A}}{3} = 62.2$. For each factor $j$, a higher $\overline{K_{ji}}$ means the level $i$ has a larger effect on La$^{3+}$ sorption. $R_j$ is defined as the range between the maximum and minimum value of $\overline{K_{ji}}$ and is used for deciding the impact of the factors.[21] It can be seen that $R_A(3.31) < R_B(3.71)$, therefore the concentration of CS$_2$ is the main influencing factor. The highest adsorption of La$^{3+}$ for each level was determined as $A_3B_2$. In Fig. 2, when [CS$_2$] = 0.5 wt%, the La$^{3+}$ adsorption amount of 0.1% ECH modified composite was much higher than that of 5% ECH modified one. $A_1B_2$ was thus selected as the optimal combination and La$^{3+}$ removal rate and adsorption capacity were 65.98% and 13.20 mg g$^{-1}$, respectively.

In order to comprehensively evaluate the differences among the mean values and to obtain the magnitudes of the factor affecting the index, the analysis of variance (ANOVA) of La$^{3+}$ removal was investigated and the calculated results are presented in Table 3. The sum of square deviation was calculated by the follow expression:

$$SS_i = 3((M_{1i} - M)^2 + (M_{2i} - M)^2 + (M_{3i} - M)^2)$$

$$(i = A, B)$$

**Table 3** Analysis of variance (ANOVA) of La$^{3+}$ removal in OA$_9$ matrix (A is wt% of ECH, B is wt% of CS$_2$)

| | | Sum of square deviation | Degrees of freedom | Mean square | F value | F, threshold value (0.1) | F, threshold value (0.05) | F, threshold value (0.01) |
|---|---|---|---|---|---|---|---|---|
| La$^{3+}$ adsorption | A | 18.47 | 2 | 9.24 | 0.75 | 4.32 | 6.94 | 18.00 |
| | B | 25.91 | 2 | 12.96 | 1.06 | 4.32 | 6.94 | 18.00 |
| | Error | 67.55 | 6 | 11.26 | — | — | — | — |
| | Sum | 93.47 | 8 | — | — | — | — | — |

The number of levels (3) subtracted 1 gave the degree of freedom 2 (DOF).[22] Sum of square deviation divided by DOF produced mean square ($M_i$). F value is defined as the ratio of the sum of the square of each factor's mean deviations to that of the experimental error. The significance of each factor is judged according to the F-distribution critical value table. $F_{0.01} < F_\alpha$ indicates that the influence of this factor is highly significant; $F_{0.05} < F_\alpha < F_{0.01}$, $F_{0.1} < F_\alpha < F_{0.05}$, and $F_\alpha < F_{0.1}$ means the factor has significant, certain effect and no significant effect, respectively. As can be seen from the Table 3, both the ECH and CS$_2$ concentrations have no significant effect on the La$^{3+}$ adsorption capacity. Further improvement in accuracy indicates that the F value of the CS$_2$ concentration has increased, but the effect is still not significant. On the other hand, the CS$_2$ concentration has certain effect on the adsorption performance, which is consistent with the results in Table 2.

## Morphologies, structures, and textural properties of samples

The morphologies of original MWCNTs, purified MWCNTs, Fe$_3$O$_4$ nanocrystals and the final Fe$_3$O$_4$@MWCNTs composites were observed by SEM (Fig. 3a–d). Relatively long and tangled MWCNTs became short and well dispersed after acid treatment. The coarsened tube walls suggest more adsorption sites are available. Fe$_3$O$_4$ cubic shaped magnetic nanoparticles with size around 3 nm were attached and embedded in the nanocomposites.

Fig. 3e shows the X-ray diffraction patterns of the purified multi-walled carbon nanotubes, Fe$_3$O$_4$ nanoparticles and the CS$_2$ functionalized MWCNT@Fe$_3$O$_4$ nanocomposites. For MWCNs, a strong graphite (002) characteristic diffraction peak corresponding to a d-spacing between graphene sheets of 3.42–3.46 Å was observed at around 25.84°. The weak (100) peak at $2\theta \approx 42.68°$ related to the in-plane graphitic structure of MWCNs.[23] These results indicate that the structure of the MWCNTs was intact after pretreatment by concentrated acids. For Fe$_3$O$_4$, six major diffraction peaks at $2\theta = 18.32°$, 31.49°, 35.34°, 44.76°, 58.13°, and 64.24° (marked by their indices $d(1\ 1\ 1)$, $d(2\ 2\ 0)$, $d(3\ 1\ 1)$, $d(4\ 0\ 0)$, $d(5\ 1\ 1)$ and $d(4\ 4\ 0)$) could be indexed to the pure cubic spinel phase of Fe$_3$O$_4$ (JCPDF card no. 19-0629).[24] Both characteristic peaks of MWCNT and main peaks of Fe$_3$O$_4$ were present, suggesting the successful embedding of Fe$_3$O$_4$ into MWCNT bundles.

## Thermogravimetric analysis

The thermogravimetric (TG) curves recorded for pristine MWCNTs, oxidized MWCNTs, and MWCNTs@Fe$_3$O$_4$ hybrid are shown in Fig. 4. The curves were measured from room temperature to 900 °C in air at heating rate of 5 °C min$^{-1}$. All samples showed <1% weight loss when the temperature was lower than 150 °C, attributing to the evolution of physically adsorbed water molecules.[25] For pristine MWCNT, differential weight loss curves showed three peaks $T_{1,max}$ at 178.8 °C, $T_{2,max}$ at 477.4 °C and $T_{3,max}$ of 868.6 °C. The DTG peak at 477.4 °C is attributed to the oxidation of disordered or amorphous carbons. At temperatures higher than 500 °C, the observed decomposition corresponds to the thermal oxidation of the remaining disordered carbon.[26] After acid treatment, the sample continuously lost 12.08% weight, due to the elimination
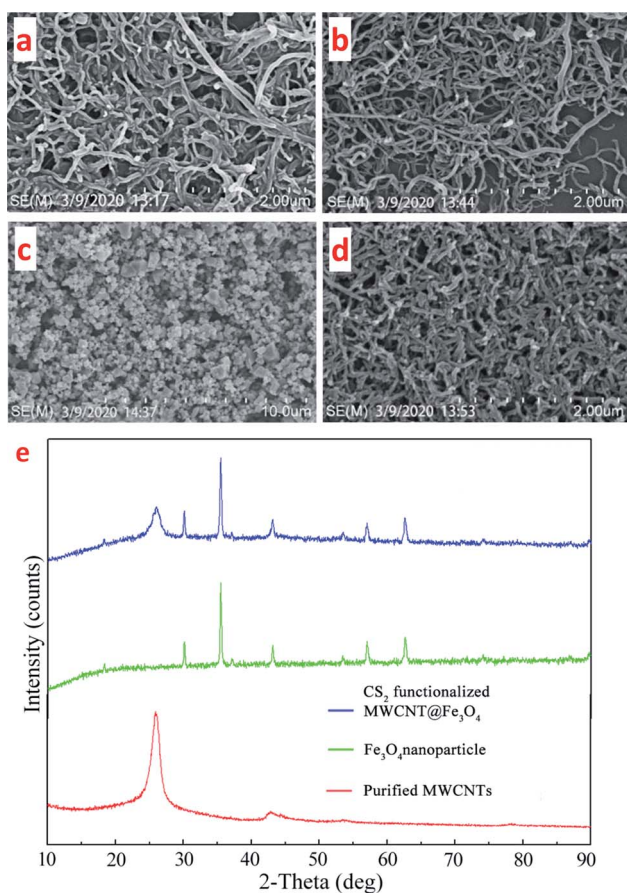
**Fig. 3** SEM images of the original MWCNTs (a), the purified MWCNTs (b), Fe$_3$O$_4$ nanoparticles (c), and CS$_2$ functionalized MWCNT@Fe$_3$O$_4$ (d). XRD patterns of the purified MWCNTs, Fe$_3$O$_4$ nanoparticles, and CS$_2$ functionalized MWCNT@Fe$_3$O$_4$ (e).
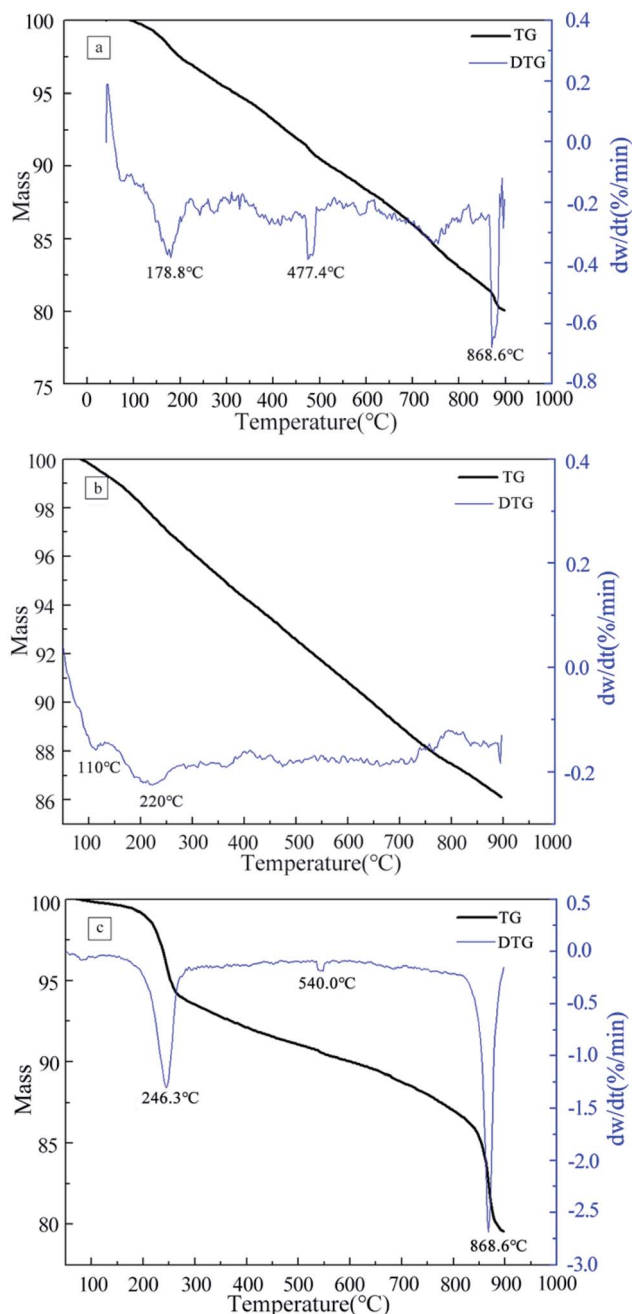
Fig. 4 TGA curves of the pristine MWCNTs (a), acid treated MWCNTs (b) and CS$_2$ functionalized MWCNTs@Fe$_3$O$_4$ (c).

volume were calculated using the Barrett–Joyner–Halenda (BJH) method as 77.39 m$^2$ g$^{-1}$ and 0.1554 cm$^3$ g$^{-1}$, respectively. The specific surface area is in the lower part of reported carbon nanotube materials, which could be explained by three factors: (1) functional groups block pore entrances; (2) bundling of nanotubes via ECH, (3) MWCNTs were partially covered with Fe$_3$O$_4$ NPs.[30,31] Moreover, the N$_2$ absorption/desorption curve at 77 K in Fig. 5 reveals a typical IV isotherm with a large H$_3$ hysteresis loop.[32] The hysteresis phenomenon is usually associated with capillary condensation in mesoporous structures.[33] Thus, slit-shaped pores are expected in these samples. The pore size distribution has a relatively wide range of 3.3 to 7.2 nm, corresponding well with the hysteresis observation.

## Fourier transform infrared (FT-IR) analysis

FT-IR characterization was performed to identify the surface functional groups. The pristine MWCNTs exhibited two major peaks at 880 and 1454 cm$^{-1}$, which could be associated with the amorphous carbon and E$_{1u}$ (1590 cm$^{-1}$) IR-active modes of graphitic C=C, respectively.[34,35] As a result of acid purification, the intensity of 880 cm$^{-1}$ band is significantly decreased. Meanwhile, the –OH band at 3444 cm$^{-1}$ and the carboxyl band
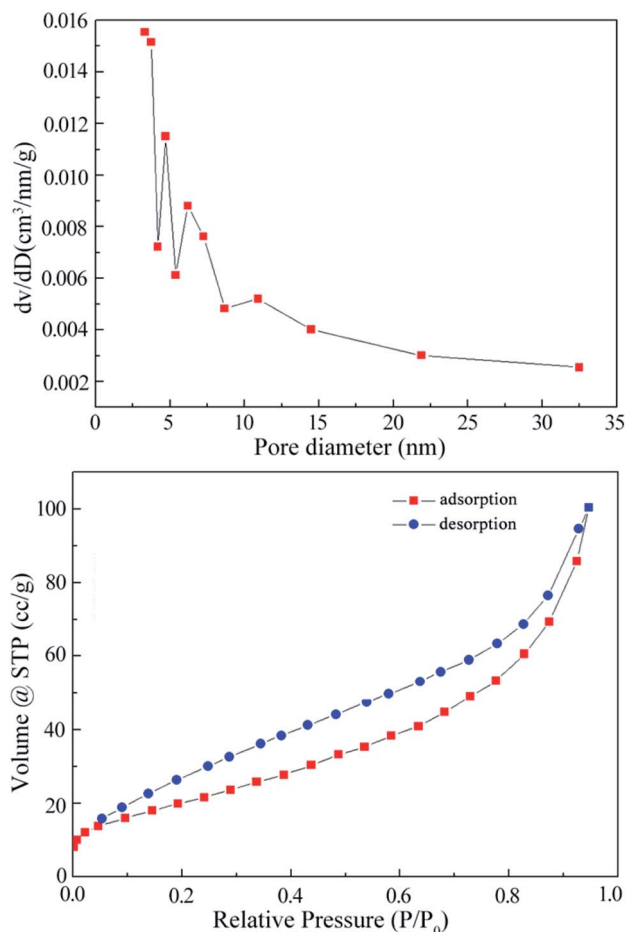


Fig. 5 N$_2$ adsorption–desorption isotherms of CS$_2$ functionalized MWCNT@Fe$_3$O$_4$.

of carboxylic and hydroxyl functional groups that attached to the MWCNT walls.[27,28] The thermal degradation of the final hybrid is a four-stage process. There is a 6.03 wt% loss at the second stage ∼200–300 °C and a 7.17 wt% loss at the fourth stage ∼800–900 °C. The former was attributed to the oxidation of the PVA and ECH while the later accounted for the degradation of CS$_2$ and Fe$_3$O$_4$.[29]

## BET analysis

To give further insight into the textural properties of the functionalized MWCNT@Fe$_3$O$_4$, the BET surface area and pore

at 1717 cm$^{-1}$ confirm the presence of hydrophilic moieties at the carbon tube surface.[36] These polar functional groups not only provide numerous ion sorption sites, but also improve the dispersity of MWCNTs in aqueous solution. The characteristic peak of pure Fe$_3$O$_4$ NPs was observed at 588 cm$^{-1}$. After mixing with MWCNTs and crosslinking by ECH, the upshifted adsorption band at 590 cm$^{-1}$ corresponds to the stretching vibration of Fe–O–Fe was revealed, confirming that Fe$_3$O$_4$ NPs were loaded onto the surface of MWCNTs through ECH coordination.[37] The successful CS$_2$ functionalization of MWCNT@Fe$_3$O$_4$ is ascertained by two peaks located at 699 cm$^{-1}$ and 1106 cm$^{-1}$, corresponding to the C–S and C=S vibrations,[38] respectively (Fig. 6).

### Surface study by X-ray photoelectron spectroscopy

To aid the interpretation, the nanocomposites were investigated by X-ray photoelectron spectroscopy (XPS) to characterize the nature of the ECH crosslinked MWCNTs and to verify the CS$_2$ functionalization on the composition of Fe$_3$O$_4$@MWCNT. The survey XPS spectra (Fig. 7a) show S, C, O, and Fe at the surface. The high resolution C 1s spectrum (Fig. 7b) shows two carbon peaks at 284.8 and 286.1 eV, respectively, indicating the presence of C=C and C=O.[39] The O 1s spectrum of the thiol-modified magnetic carbon nanotubes can be successfully fit to three main peaks (Fig. 7c), which are located at the binding energies of 530.2, 532.2, and 533.5 eV, corresponding to C–O, C–OH and C=O–OH in the carboxyl group.[40] The introduction of these oxygen-containing functional groups on the surface of the carbon nanotubes is expected to improve the dispensability. The Fe 2p core level spectrum (Fig. 7d) shows two binding energies at 711.3 and 724.7 eV, which can be assigned to Fe 2p$_{3/2}$ and Fe 2p$_{1/2}$ components. These values correlate well with those of bulk Fe$_3$O$_4$.[41,42] Fig. 7e exhibits two S 2p peaks at 164.8 eV and
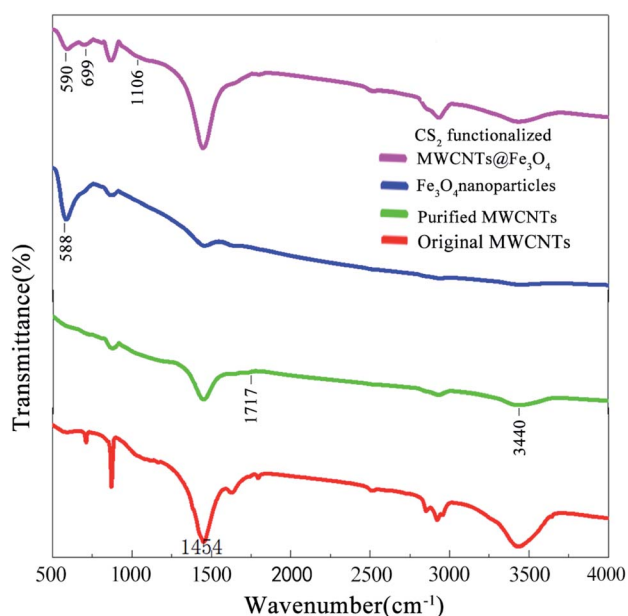


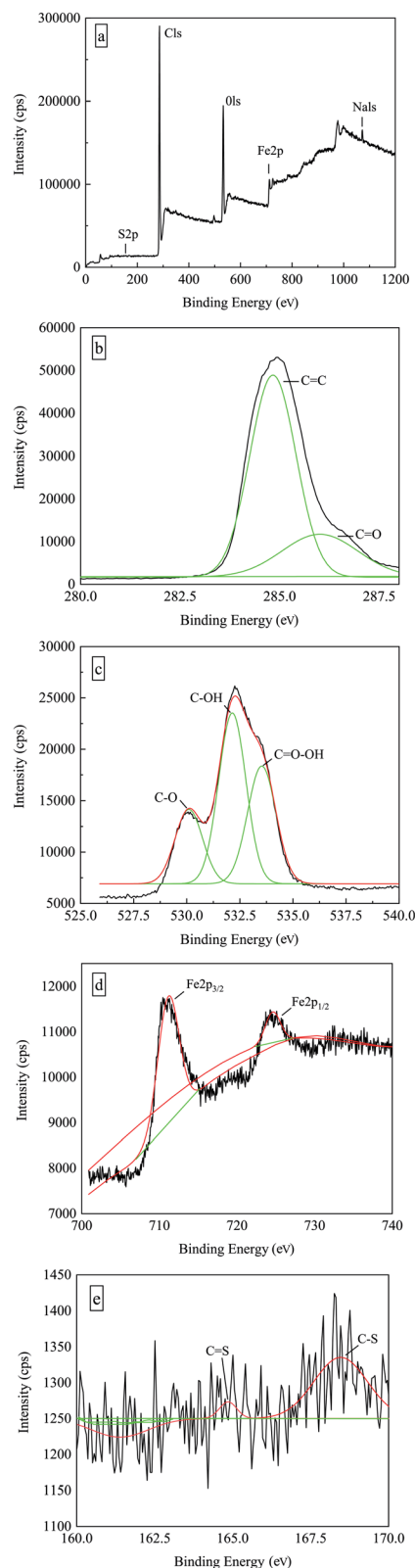Fig. 6 Fourier transform infrared (FT-IR) spectra of various samples.



Fig. 7 XPS spectra of various samples. The survey XPS spectra (a), the high resolution C 1s spectrum (b), the high resolution O 1s spectrum (c), the Fe 2p core level spectrum (d), the high resolution S 2p spectrum (e).

168.5 eV, corresponding to the C–S and S=O bonds, further confirming the presence of thiol groups on the surface of composites.[43,44]

Previous studies have confirmed that the pore size distribution and surface functional groups are important factors that determine the REE adsorption performance of nano-carbons. In this study, as revealed by the BET, FTIR and XPS characterizations, the mesoporous structure and the presence of carboxyl and S groups contributed to the $La^{3+}$ adsorption.

### VSM analysis

Magnetization curves of MWCNT@$Fe_3O_4$ before and after $CS_2$ modification are presented in Fig. 8. $CS_2$ modification decreased both the saturation magnetization ($M_s$) from 21.37 to 17.22 and the remanence ($M_r$) from 3.34 to 2.55 emu $g^{-1}$. The coercivity was decreased from 114.42 to 111.36 Oe. The magnetic separation feasibility of final MWCNT@$Fe_3O_4$ was tested by placing a magnet near a test tube containing the nanohybrids. As shown in the inset, the samples can easily be

dispersed in water and an external magnet can attract them for later removal. The data illustrates that the magnetite nanoparticles, tethered on the surface of the MWCNTs give the adsorbent a magnetic response.

The sequential adsorption–desorption cycles showed that MWCNT@$Fe_3O_4$ had acceptable reusability. As shown in Table S1,† after two acid elution processes, the adsorption capacity of $La^{3+}$ dropped slightly from 23.23 to 19.32 mg $g^{-1}$. The adsorbents maintained similar XRD patterns. FTIR spectra indicated the existence of carboxyl, Fe–O–Fe, C–S and C=S groups. The decrease of adsorption efficiency can be mainly attributed to a progressive saturation of the adsorbent active sites by $La^{3+}$ as well as negative impact on material integrity due to extreme pH levels.

## Conclusions

In this study, uniform $Fe_3O_4$ nanoparticles were embedded into multi-wall carbon nanotube (MWCNT) bundles *via* a facile epichlorohydrin (ECH) cross-linking process. The nanocomposites were further functionalized by $CS_2$ as a reusable magnetic adsorbent for enhanced rare earth $La^{3+}$ adsorption in aqueous media. The maximum adsorption capacity was found to vary with ECH and $CS_2$ concentrations. The best concentration combination for favourable $La^{3+}$ adsorption was determined by orthogonal array analysis and experimental results. Different characteristics of the final absorbent are explored through FESEM, XRD, TGA, BET, FTIR, XPS, and VSM methods. This retrievable nano adsorbent has exhibited suitable efficiency in $La^{3+}$ recovery and made the process highly valuable from environmental perspective.

## Funding

## Conflicts of interest

There are no conflicts to declare.

## Acknowledgements

## References

1  G. Charalampides, K. I. Vatalis, B. Apostoplos and B. Ploutarch-Nikolas, *Procedia Economics and Finance*, 2015, **24**, 126–135.
2  J. C. Callura, K. M. Perkins, C. W. Noack, N. R. Washburn, D. A. Dzombak and A. K. Karamalidis, *Green Chem.*, 2018, **20**(7), 1515–1526.
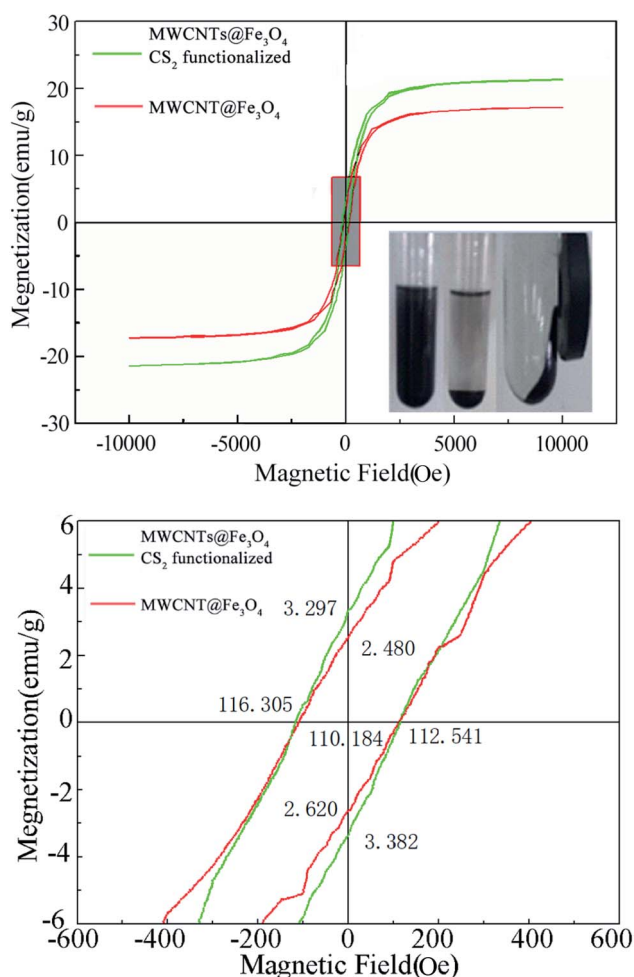


Fig. 8  Magnetizations *versus* applied magnetic field for the magnetic carbon nanotubes. Curves were recorded at 298 K. The insets are photographs of magnetic carbon nanotubes in the presence (right image) and in the absence (left image) of a magnet.

3 X. J. Yang, A. Lin, X. L. Li, Y. Wu, W. Zhou and Z. Chen, *Environ. Dev.*, 2013, **8**, 131–136.

4 G. A. Moldoveanu and V. G. Papangelakis, *Hydrometallurgy*, 2012, **117**, 71–78.

5 T. Kegl, A. Košak, A. Lobnik, Z. Novak, A. K. Kralj and I. Ban, *J. Hazard. Mater.*, 2020, **386**, 121632.

6 D. Dupont, W. Brullot, M. Bloemen, T. Verbiest and K. Binnemans, *ACS Appl. Mater. Interfaces*, 2014, **6**, 4980–4988.

7 C. E. Cardoso, J. C. Almeida, C. B. Lopes, T. Trindade, C. Vale and E. Pereira, *Nanomaterials*, 2019, **9**, 814.

8 S. M. A. Koochaki-Mohammadpour, M. Torab-Mostaedi, A. Talebizadeh-Rafsanjani and F. Naderi-Behdani, *J. Dispersion Sci. Technol.*, 2014, **35**, 244–254.

9 X. Xu, J. Zou, X. R. Zhao, X. Y. Jiang, F. P. Jiao, J. G. Yu and J. Teng, *Colloids Surf., A*, 2019, **570**, 127–140.

10 Z. N. Huang, X. L. Wang and D. S. Yang, *Water Sci. Eng.*, 2015, **8**, 226–232.

11 G. D. Tarigh and F. Shemirani, *Talanta*, 2013, **115**, 744–750.

12 W. W. Tang, G. M. Zeng, J. L. Gong, Y. Liu, X. Y. Wang, Y. Y. Liu and D. Z. Tu, *Chem. Eng. J.*, 2012, **211**, 470–478.

13 J. L. Gong, B. Wang, G. M. Zeng, C. P. Yang, C. G. Niu, Q. Y. Niu and Y. Liang, *J. Hazard. Mater.*, 2009, **164**, 1517–1522.

14 X. Wang, Z. J. Ma, L. L. Chai, L. Q. Xu, Z. Y. Zhu, Y. Hu, J. J. Qian and S. M. Huang, *Carbon*, 2019, **141**, 643–651.

15 T. T. Li, J. J. Qian, Q. Q. Zhou, J. L. Lin and Y. Q. Zheng, *Dalton Trans.*, 2017, **46**, 13020.

16 X. Wang, A. Dong, Z. Y. Zhu, L. L. Chai, J. Y. Ding, L. Zhong, T. T. Li, Y. Hu, J. J. Qian and S. M. Huang, *Small*, 2020, **16**, 2004614.

17 M. J. Manos and M. G. Kanatzidis, *Chem. Sci.*, 2016, **7**, 4804–4824.

18 L. Dehabadi and L. D. Wilson, *Carbohydr. Polym.*, 2014, **113**, 471–479.

19 I. A. Udoetok, R. M. Dimmick, L. D. Wilson and J. V. Headley, *Carbohydr. Polym.*, 2016, **136**, 329–340.

20 D. Saha, S. Barakat, S. E. Van Bramer, K. A. Nelson, D. K. Hensley and J. Chen, *ACS Appl. Mater. Interfaces*, 2016, **8**, 34132–34142.

21 X. Wu and D. Y. Leung, *Appl. Energy*, 2011, **88**, 3615–3624.

22 J. Luo, G. Zhu, F. Zhang, Q. Li, T. Zhao and X. Zhu, *RSC Adv.*, 2015, **5**, 6071–6078.

23 Y. Li, X. B. Zhang, X. Y. Tao, J. M. Xu, W. Z. Huang, J. H. Luo and H. J. Geise, *Carbon*, 2005, **43**, 295–301.

24 L. Cui, H. Huang, P. Ding, S. Zhu, W. Jing and X. Gu, *Sep. Purif. Technol.*, 2020, **237**, 116380.

25 V. Datsyuk, M. Kalyva, K. Papagelis, J. Parthenios, D. Tasis, A. Siokou and C. Galiotis, *Carbon*, 2008, **46**, 833–840.

26 P. Hou, C. Liu, Y. Tong, S. Xu, M. Liu and H. Cheng, *J. Mater. Res.*, 2001, **16**, 2526–2529.

27 M. Tang, H. Dou and K. Sun, *Polymer*, 2006, **47**, 728–734.

28 S. Grandi, A. Magistris, P. Mustarelli, E. Quartarone, C. Tomasi and L. Meda, *J. Non-Cryst. Solids*, 2006, **352**, 273–280.

29 S. H. Chaki, T. J. Malek, M. D. Chaudhary, J. P. Tailor and M. P. Deshpande, *Adv. Nat. Sci.: Nanosci. Nanotechnol.*, 2015, **6**, 035009.

30 A. Peigney, C. Laurent, E. Flahaut, R. R. Bacsa and A. Rousset, *Carbon*, 2001, **39**, 507–514.

31 M. E. Birch, T. A. Ruda-Eberenz, M. Chai, R. Andrews and R. L. Hatfield, *Ann. Occup. Hyg.*, 2013, **57**, 1148–1166.

32 N. Yan, X. Zhou, Y. Li, F. Wang, H. Zhong, H. Wang and Q. Chen, *Sci. Rep.*, 2013, **3**, 16.

33 A. A. Farghali, H. A. Tawab, S. A. Moaty and R. Khaled, *J. Nanostruct. Chem.*, 2017, **7**, 101–111.

34 J. L. Bantignies, J. L. Sauvajol, A. Rahmani and E. Flahaut, *Phys. Rev. B: Condens. Matter Mater. Phys.*, 2006, **74**, 195425.

35 U. J. Kim, X. M. Liu, C. A. Furtado, G. Chen, R. Saito, J. Jiang and P. C. Eklund, *Phys. Rev. Lett.*, 2005, **95**, 157402.

36 L. Stobinski, B. Lesiak, L. Kövér, J. Tóth, S. Biniak, G. Trykowski and J. Judek, *J. Alloys Compd.*, 2010, **501**, 77–84.

37 M. Moazzen, A. M. Khaneghah, N. Shariatifar, M. Ahmadloo, I. Eş, A. N. Baghani and N. Rastkari, *Arabian J. Chem.*, 2019, **12**, 476–488.

38 C. N. R. Rao, R. Venkataraghavan and T. R. Kasturi, *Can. J. Chem.*, 1964, **42**, 36–42.

39 D. L. Ramasamy, V. Puhakka, B. Doshi, S. Iftekhar and M. Sillanpää, *Chem. Eng. J.*, 2019, **365**, 291–304.

40 J. V. Rojas, M. Toro-Gonzalez, M. C. Molina-Higgins and C. E. Castano, *Mater. Sci. Eng., B*, 2016, **205**, 28–35.

41 H. Veisi, S. Najafi and S. Hemmati, *Int. J. Biol. Macromol.*, 2018, **113**, 186–194.

42 Y. Chu, X. Tan, Z. Shen, P. Liu, N. Han, J. Kang and S. Liu, *J. Hazard. Mater.*, 2018, **356**, 53–60.

43 A. A. Razzaq, Y. Yao, R. Shah, P. Qi, L. Miao, M. Chen and Z. Deng, *Energy Storage Mater.*, 2019, **16**, 194–202.

44 I. Menapace, W. Yiming and E. A. Masad, *Advances in Materials and Pavement Performance Prediction*, Taylor & Francis Group, London, 2018, p. 431, ISBN 978-1-138-31309-5.